Supplemental Material

Supplemental Methods

Adoptive T Cell Transfer

For adoptive T cell transfer, freshly isolated splenocytes, from either congenically marked wild-type mice ($CD45.1^+$) or $TSLPR^{-/-}$ mice, first underwent $CD4^+$ cell selection using magnetic beads microbeads and MACS column isolation (Miltinyi Biotec Inc.), $CD4^+$ T cells were sorted using a FACS ARIA II (BD Bioscience, San Jose, CA). Recipient mice were irradiated with a sublethal dose of irradiation (400 cGy) prior to adoptive T cell transfer and injected intravenously with 2 x 10^6 $CD4^+$ T cells.

Primary Pancreatic Tumor Transfer

Primary pancreatic tumor cells were obtained from $P48^{+/Cre}$;LSL-$KRAS^{G12D}$;$p53^{flox/+}$ donor mice (2). Spontaneous pancreatic tumors formed in the donor animals were harvested as soon as the tumors were palpable on the abdominal exam (<2cm in diameter) and implanted subcutaneously into the right flank of Wt animals for further tumor expansion. Single cell pancreatic tumor suspension was then prepared from implanted tumors as they reached 1.5cm in diameter and meshed through a new 70 micron filter as outlined in primary breast tumor transfer method. 2 x 10^6 cells were injected per mouse into the Wt and K14-$TSLP^{tg}$ animals' right flank at D0 and mice were monitored for the rate of tumor growth over time.

Flow Cytometry

Peripheral blood was obtained and treated with red blood cell lysis solution. Single cells suspensions were prepared from lymph node. To obtain lymphocytes within breast tumors, the tumors were harvested and tumor-infiltrating leukocytes were isolated as stated above for obtaining primary breast tumor cells except $CD45^+$ Microbeads were used for isolation (Miltinyi

Biotec Inc.). Prior to staining cells with fluorochrome-conjugated antibodies, all cells were treated with 2.4G2 supernatant. The following monoclonal surface antibodies were used for analysis: CD3e (145-2C11, eBioscience, San Diego, CA), CD4 (RM4-5, eBioscience), CD8a (53-6.7, eBioscience), CD19 (eBio1D3, eBioscience), CD44 (IM7, eBioscience), CD62L (MEL-14, eBioscience) PD-1 (J43, eBioscience), CD45.1 (A20, eBioscience), MHCII (M5/114.15.2, BD Pharmingen), CD11c (N418, eBioscience), CD11b (M1/70, BioLegend, San Diego, CA), F4/80 (BM8, eBioscience), FasL (MFL3, eBioscience), NKG2D (CX5, eBioscience), and CD107a (eBio1D4B, eBioscience). Intracellular stains were performed after fixation and permeabilization with Foxp3/Transcription Factor Staining Buffer Set (eBioscience). The following antibodies were used for intracellular stains: GATA3 (TWAJ, eBioscience), Foxp3 (FJK-16s, eBioscience), T-bet (eBio4B10, eBioscience), Granzyme B (NGZB, eBioscience) and Ki-67 (SolA15, eBioscience). All flow cytometry data was collected using a FACS Canto flow cytometer (BD Bioscience) and analyzed using FlowJo software (Tree Star, Ashland, OR).

Histology, Immunofluorescence, and Immunohistochemistry

All histology samples were harvested and fixed in 2% paraformaldehyde-lysine-phosphate fixative (PLP) for 6 hours followed by 30% sucrose solution overnight at 4°C. Samples were both frozen in OCT freezing medium (Sakura Finetek, Torrance, CA) or processed and embedded in paraffin. Frozen samples were sectioned at 9μm, mounted on glass slides, and incubated with anti-mouse CD3 (Polyclonal, Abcam, Cambridge, MA), CD4 (RM4-5, eBioscience), CD8 (eBioH35-17.2, eBioscience), MHCII (AF6-120.1, eBioscience), Mcpt8 (TUG8, BioLegend), B220 (CD45R, RA3-6B2, BioLegend), CD11b (M1/70, BioLegend), CD11c (N418, eBioscience), F4/80 (BM8, eBioscience), biotin-conjugated anti-TSLP (Polyclonal, R&D Systems, Minneapolis, MN) followed with FITC-conjugated streptavidin, biotin-conjugated anti-Cytokeratin 14 (LL002, Thermo Fisher Scientific Inc., Waltham, MA) followed with APC-

conjugated streptavidin & purified rabbit anti-cytokeratin (DAKO, Carpinteria, CA) followed with APC-conjugated anti-rabbit antibody. DAPI nuclear stain (Vector Labs, Burlingame, CA) was used to counterstain sections. Paraffin embedded tissues were sectioned at 5μm and stained for Hematoxylin and eosin (H&E) and toluidine blue. Immunohistochemistry was performed on paraffin embedded tissue by Digestive Disease Research Core Center (Washington University, Saint Louis, MO) for CD3, CD45, and pan-cytokeratin stains. Histology images were taken using fluorescent microscope or NanoZoomer (Hamamatsu Photonics K.K., Japan).

Genotyping

PCR was used fro detection of K14-TSLP and PyMT transgenes and *Tslpr* wild-type and mutant alleles. The following primer pairs were used to genotype mice (all primers shown are 5' to 3':

K14-TSLP^{tg} Fwd - TCATCCTGCAAGTACTAGTACGGATGGGGC and

Rev-TGTTTTGGACTTCTTGTGCCATTTCCTGAG,

PyMT^{tg} – Fwd - ATACTGCTGGAAGAAGACGAAATCCTTG and Rev - CTCTGTGAGTAGCTCTCATTCTCTGACTC,

Tslpr^{+} - Fwd - TGAACCAGTCATGGTCTGGGATGATCTTGC and Rev - TCATGAACGACCACTTCCTATGTTGGACACG,

Tslpr^{-} - Fwd - AGCGTTGGCTACCCGTGATATTGCTGAAGAG and

Rev –TCATGAACGACCACTTCCTATGTTGGACACG

qRT-PCR

All cDNA samples from skin, lymph node, breast tumor, and breast gland were prepared as previously reported (1). The following primer sets were used for SYBR green analysis (all primers are shown 5` to 3`): *Tslp* Fwd - CCAGGCTACCCTGAAACTGA, *Tslp* Rev - TCTGGAGATTGCATGAAGGA, *Il5* Fwd – CTCTGTTGACAAGCAATGAGACG, *Il5* Rev – TCTTCAGTATGTCTAGCCCCTG, *Il10* Fwd – GCTCTTACTGACTGGCATGAG, *Il10* Rev –

CGCAGCTCTAGGAGCATGTG, *Ifng* Fwd - GATATCTGGAGGAACTGGCAAAAG, *Ifng* Rev – AGAGATAATCTGGCTCTGCAGGAT, *Tnf* Fwd – CCCTCACACTCAGATCATCTTCT, *Tnf* Rev – GCTACGACGTGGGCTACAG, *Il9* Fwd – ATGTTGGTGACATACATCCTTGC, *Il9* Rev – TGACGGTGGATCATCCTTCAG, *Il13* Fwd – CCTGGCTCTTGCTTGCCTT, *Il13* Rev – GGTCTTGTGTGATGTTGCTCA, *Il1b* Fwd – TGACGGACCCCAAAAGATGA, *Il1b* Rev – TGCTGCTGCGAGATTTGAAG, *Tgfb1* Fwd – GCTGAACCAAGGAGACGGAAT, *Tgfb1* Rev – CAAGAGCAGTGAGCGCTGAA, *Vegfa* Fwd – CCCACGACAGAAGGAGAGCAGAAGT, *Vegfa* Rev – CATCAGCGGCACACAGGACGG, *Il6* Fwd – AGGCGCCCAACTGTGCTAT, *Il6* Rev – TCTCCTGCGTGGAGAAAAGG, *Cxcl5* (*Il8*) Fwd – CGGCAATGAAGCTTCTGTAT, *Cxcl15* (*Il8*) Rev – CCTTGAAACTCTTTGCCTCA, and *Gapdh* Fwd - GGTCCTCAGTGTAGCCCAAG, *Gapdh* Rev - AATGTGTCCGTCGTGGATCT. PrimeTime Assays (Integrated DNA Technologies, USA, Coralville, Iowa) were used for TaqMan analysis: *Il4* - Mm.PT.28.32703659, *Il17a* - Mm.PT.58.6531092, *Il23a* - Mm.PT.581059418.g, *Il33* - Mm.PT.58.45991004, and *Gapdh* - Mm.PT.39a.1. All transcript levels were normalized to *gapdh* levels.

Carmine Staining

Mammary tissue was harvested from 15 week old wild-type, K14-TSLP^{tg}, PyMT^{tg}, or K14-TSLP^{tg};PyMT^{tg}, and placed on glass microscope slide to appear as close as possible the arrangement of the tissue in the mouse. The glands were immediately fixed overnight in Carnoy's Solution (3:1 mixture of 100% ethanol and glacial acidic acid) at 4°C. Next, the tissue was hydrated through graded alcohol. The glands were then stained in Carmine Alum (Stem Cell Technologies, Vancouver, BC, Canada) overnight at 4°C. The tissues were then rinsed in deionized water and dehydrated and cleared in xylene before mounting with a coverslip.

ELISA

Serum TSLP levels were determined using BioLegend Max Mouse TSLP ELISA kit according to manufacturer's instructions (BioLegend, San Diego, CA).

Supplemental Figures

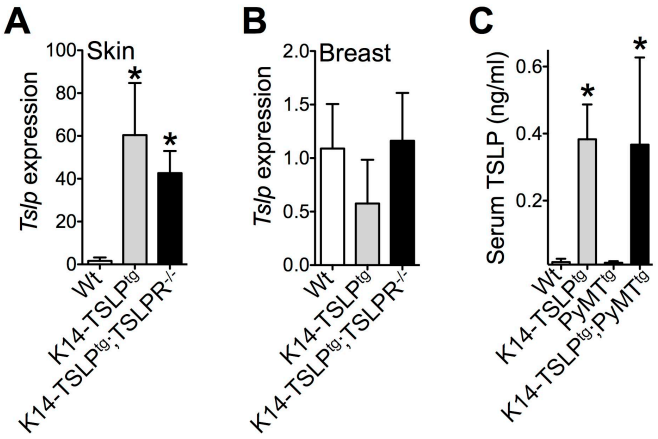

Supplemental Figure 1. K14-TSLP transgene is expressed in the skin, which leads to elevated circulating levels of TSLP. (**A**) Bar graph showing the relative expression of *Tslp* versus *Gapdh* in the skin of 10-week-old K14-TSLP^{tg} and K14-TSLP^{tg};TSLPR$^{-/-}$ animals compared to their wild-type (Wt) littermates (n = 4 per group; *: $p < 0.05$ compared to Wt, student's *t*-test). (**B**) K14-TSLP transgene is not expressed in the breast gland. Bar graph showing the relative expression of *Tslp* versus *Gapdh* in the breast glands isolated from 10-week-old K14-TSLP^{tg} and K14-TSLP^{tg};TSLPR$^{-/-}$ animals mice compared to their wild-type (Wt) littermates (n = 4 per group). Note that the Y-axis in "A" shows a much higher magnitude of expression compared to "B". (**C**) TSLP overexpression in the skin results in elevated circulating TSLP levels. Bar graph demonstrating the serum TSLP levels in 10-week-old Wt, K14-TSLP^{tg}, PyMT^{tg} and K14-TSLP^{tg};PyMT^{tg} female mice (n = 4 per group; *: $p < 0.05$ compared to Wt, student's *t*-test).

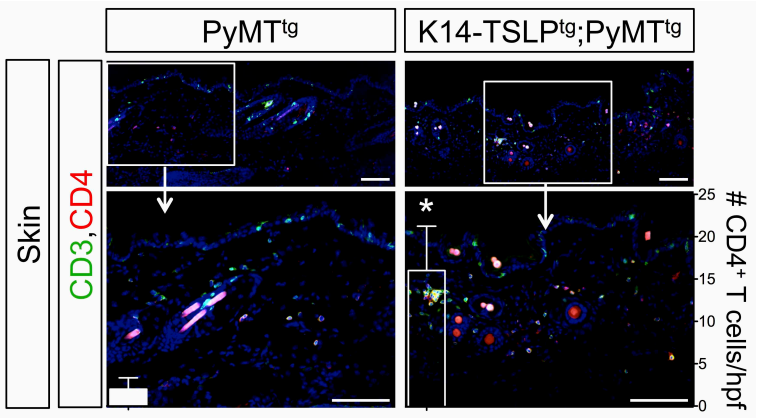

Supplemental Figure 2. Accumulation of $CD4^+$ T cells in the inflamed skin of K14-$TSLP^{tg}$;$PyMT^{tg}$ compared to normal skin of $PyMT^{tg}$ animals. Representative images are shown with higher magnification of insets indicated at the bottom. The average number of $CD4^+$ T cells in 10 random high power fields (hpf) in skin are shown as bar graphs next to the images (*: $p < 0.05$ compared to $PyMT^{tg}$, student's *t*-test; scale bars = 100μm).

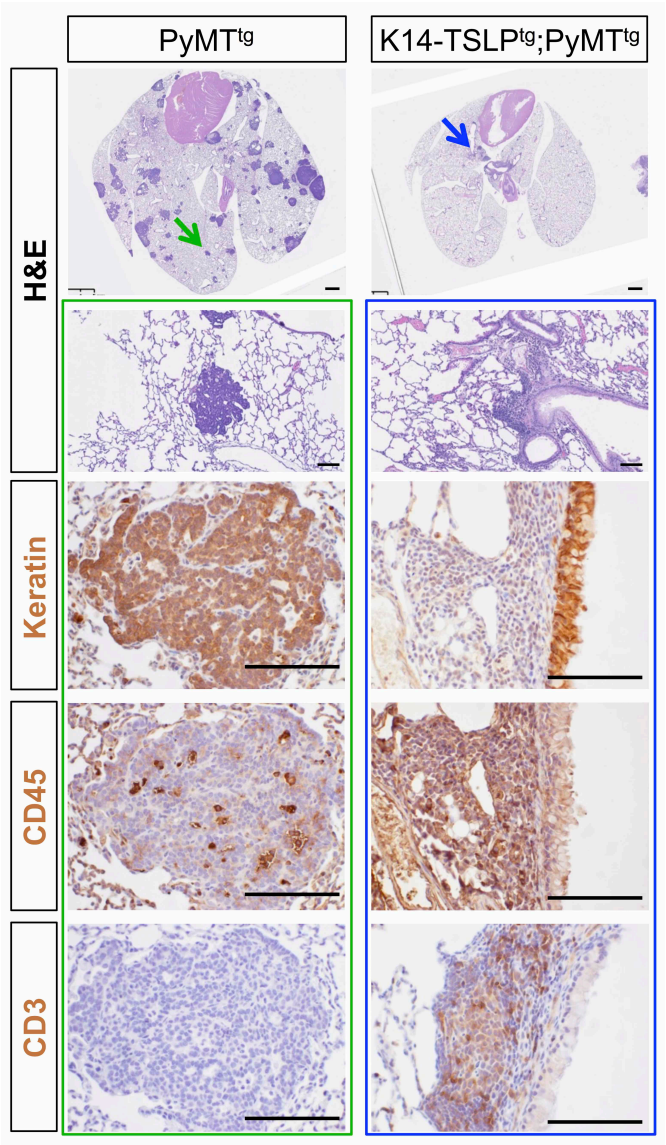

Supplemental Figure 3. No breast cancer metastasis is found in K14-TSLP^{tg};PyMT^{tg} lungs while there are several metastatic foci present in PyMT^{tg} lungs. Representative images demonstrate the presence of pauci-inflammatory collection of cytokeratin-positive epithelial cells in PyMT^{tg} lung while the cellular collections near the airways in K14-TSLP^{tg};PyMT^{tg} lungs are inflammatory infiltrates associated with atopic march in K14-TSLP^{tg};PyMT^{tg} animals. Arrows point to the areas that are shown in magnified images (Scale bars: Whole lung images = 1mm, close-up images = 100μm).

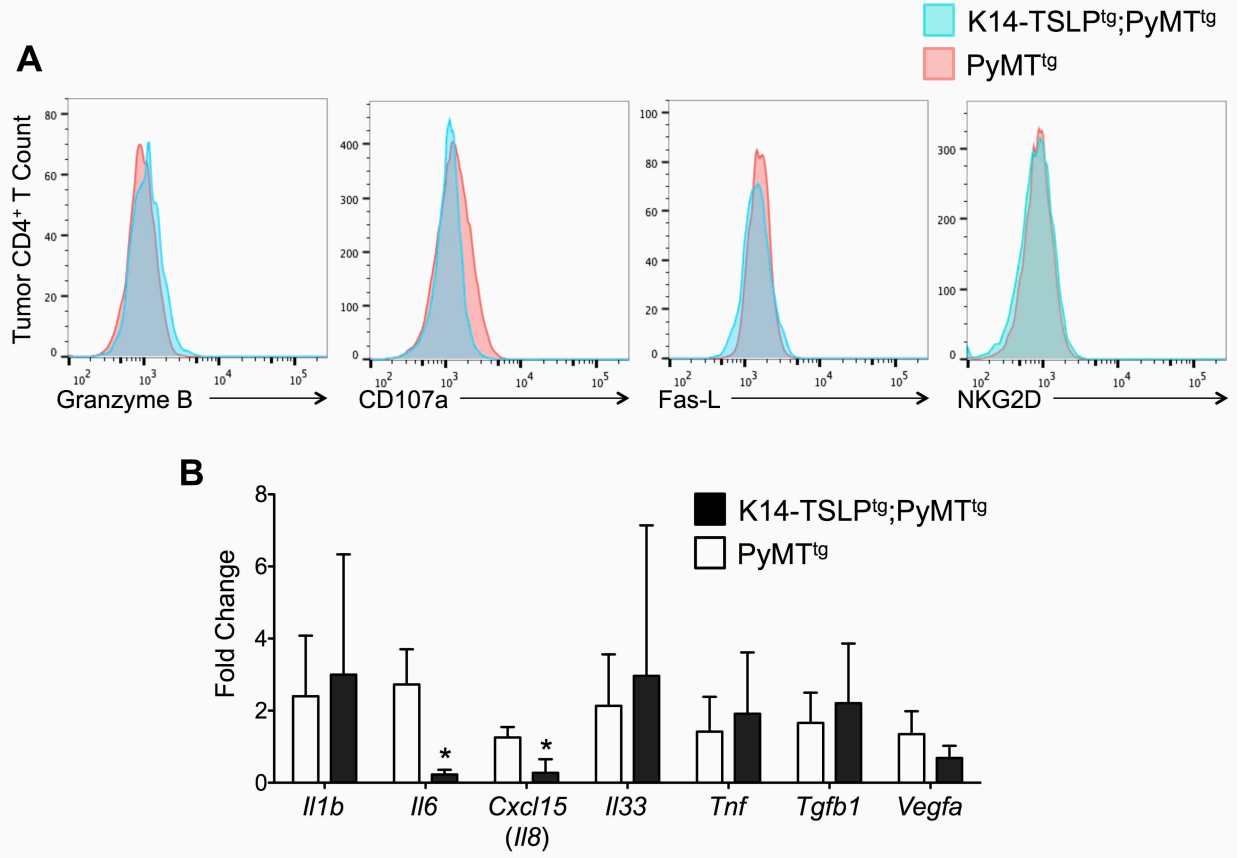

Supplemental Figure 4. TSLP induction suppresses the expression of pro-tumorigenic factors in the breast. (**A**) Characterization of breast tumor-infiltrating CD4$^+$ T lymphocytes for the expression of cytotoxic factors and degranulation. Representative flow cytometry histograms demonstrate the absence of the cytotoxic factors or degranulation (CD107a) among CD4$^+$ T cells isolated from PyMT^{tg} and K14-TSLP^{tg};PyMT^{tg} tumors cells. (**B**) Bar graphs show the relative mRNA expression of several tumor-promoting factors versus *Gapdh* in K14-TSLP^{tg};PyMT^{tg} breast tumors compared to PyMT^{tg} (n $\geq$ 4 per group; *: $p < 0.05$ compared to PyMT^{tg}, student's *t*-test).

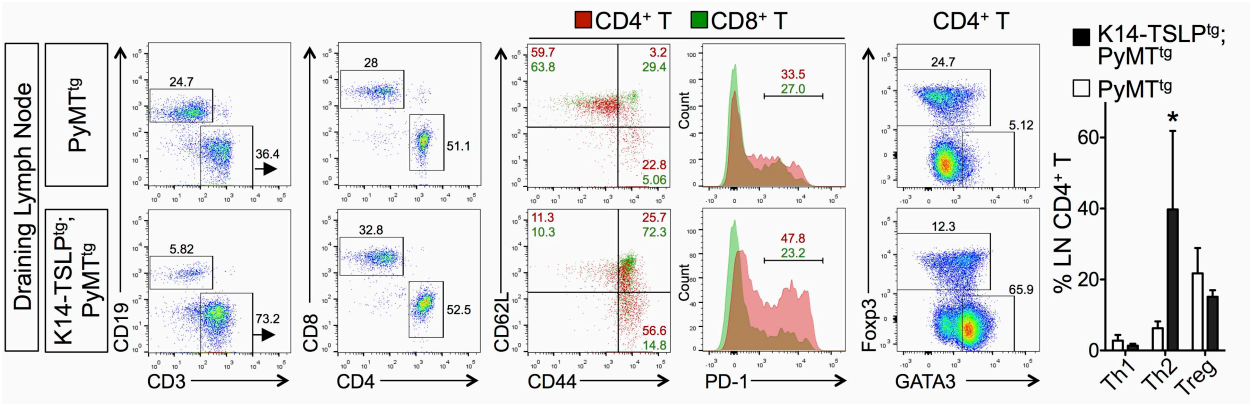

Supplemental Figure 5. Characterization of lymphocytes within the tumor draining lymph nodes demonstrates that TSLP overexpression mainly causes the activation and expansion of Th2 cells. Representative flow cytometry plots demonstrate the percentage of B cells, $CD4^+$ and $CD8^+$ T cells in $PyMT^{tg}$ and $K14\text{-}TSLP^{tg}$;$PyMT^{tg}$ tumor draining lymph nodes. CD44/CD62L and PD-1 stains determine the activation status of T cells. GATA3 and Foxp3 transcription factor stains demonstrate the polarization status of $CD4^+$ T cells. Bar graph shows the percentage of T-bet^+ Th1, $GATA3^+$ Th2 and $Foxp3^+$ T regulatory cells (Tregs) in the tumor draining lymph nodes of $PyMT^{tg}$ and $K14\text{-}TSLP^{tg}$;$PyMT^{tg}$ animals ($n > 4$ per group; *: $p < 0.05$ compared to $PyMT^{tg}$, student's *t*-test).

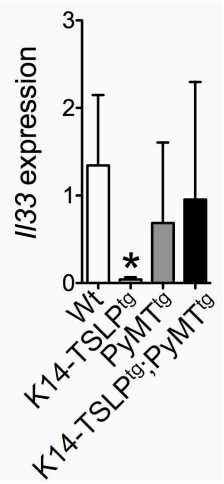

Supplemental Figure 6. IL-33 is not increased in response to TSLP induction in the breast tumors. Bar graph showing the relative expression of *Il33* versus *Gapdh* in the breast glands/tumors isolated from mice listed (n = 4 per group; *: $p < 0.05$ compared to Wt, student's *t*-test).

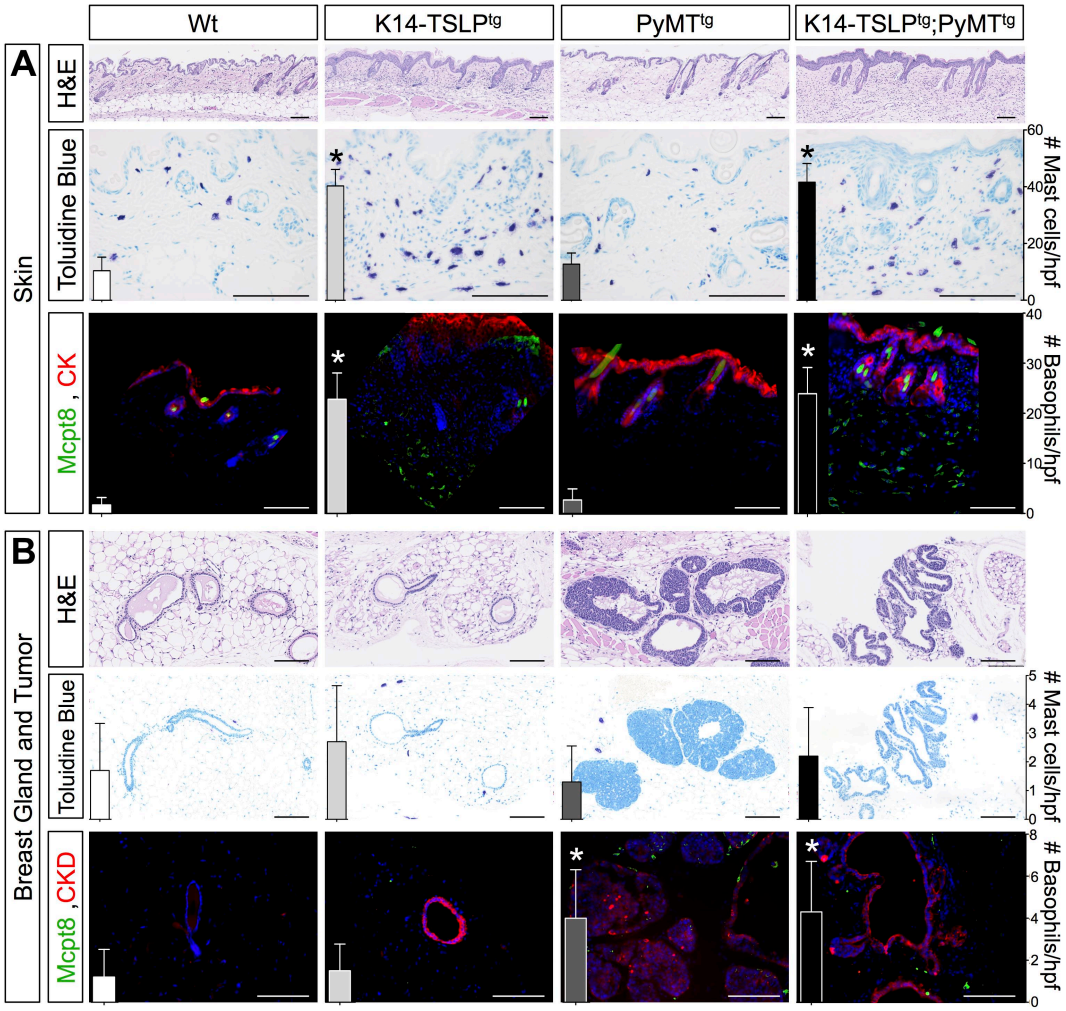

Supplemental Figure 7. Systemic TSLP expression does not impact mast cell or basophil accumulation in the breast cancer. (**A**) Histological analysis of the skin from Wt, K14-TSLP^{tg}, PyMT^{tg} and K14-TSLP^{tg};PyMT^{tg} mice reveals the accumulation of mast cells (toluidine blue positive cells) and basophils (Mcpt8^{+}) in inflamed skin of TSLP-expressing animals. However, this skin allergic inflammation does not affect the breast and breast glands/tumors of the animals. H&E and toluidine blue-stained images appear in Figure 1D. (**B**) 10-week-old K14-TSLP^{tg} and K14-TSLP^{tg};PyMT^{tg} female breast glands/tumors contain similarly low density of mast cells and basophils as their Wt and PyMT^{tg} counterparts. Note a small but significant increase in the number of basophils in both PyMT^{tg} and K14-TSLP^{tg};PyMT^{tg} breast tumors compare to Wt and K14-TSLP^{tg} breast glands. H&E-stained images appear in Figure 1F.

Representative images are shown. The average number of mast cells and basophils in 10 random high power fields (hpf) are shown as bar graphs next to each image (*: $p < 0.05$ compared to Wt mice, student's *t*-test; scale bars = 100μm).

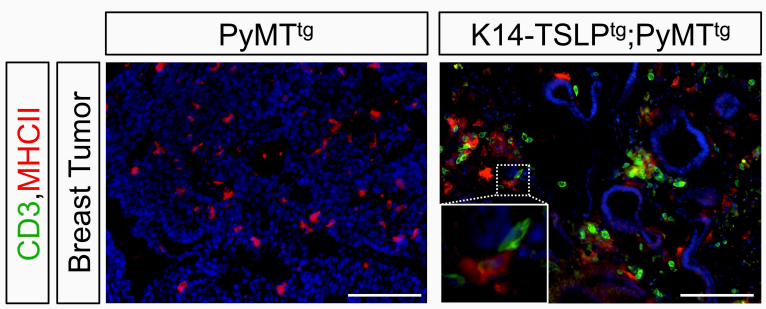

Supplemental Figure 8. Presence of large number of MHCII^{+} antigen presenting cells in the breast adenomas of K14-TSLP^{tg};PyMT^{tg} mice. Note the accumulation of T cells in the K14-TSLP^{tg};PyMT^{tg} breast tumors in close contact with MHCII^{+} APCs residing adjacent to the dilated mammary ducts. Representative images are shown (Scale bars = 100μm).

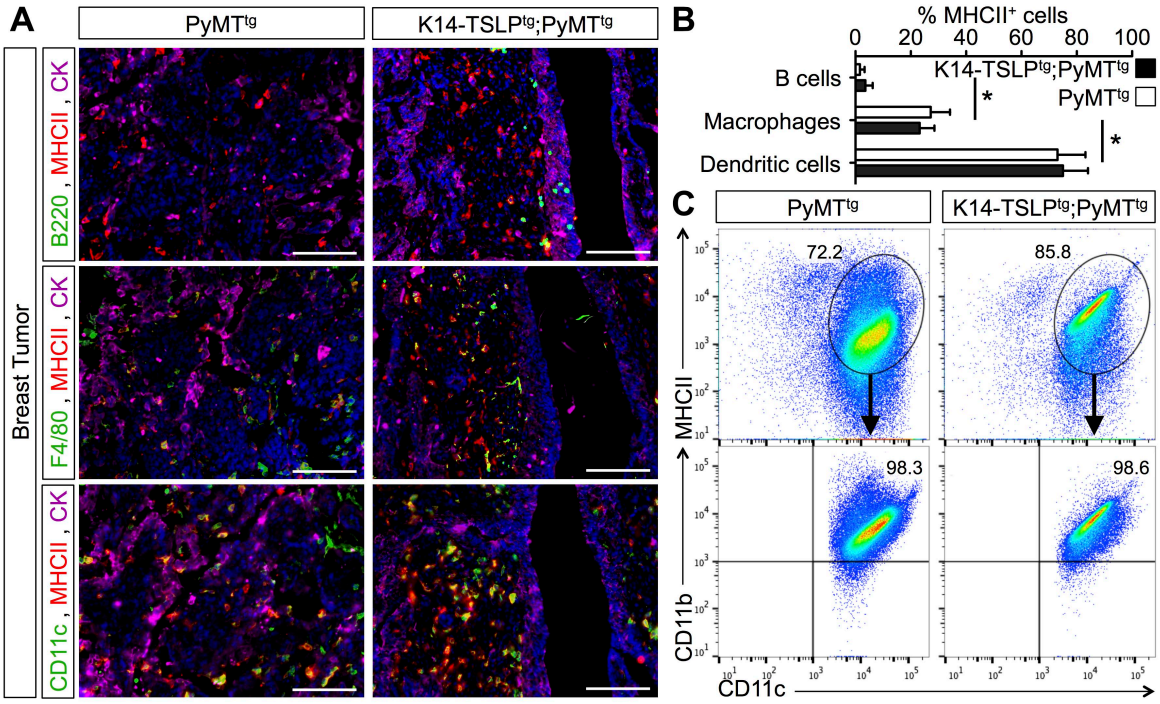

Supplemental Figure 9. Conventional dendritic cells (DC) constitute the majority of antigen presenting cells in PyMT breast cancers. (**A**) Endpoint histological analysis reveals the density of MHCII^{+} B cells (B220), macrophages (F4/80) and dendritic cells (CD11c) in breast tumors of PyMT^{tg} and K14-TSLP^{tg};PyMT^{tg} female mice. Representative images show immunofluorecent stains of adjacent sections of breast tumors (scale bars = 100μm). (**B**) Bar graph showing percent MHCII^{+} cells within the breast tumors that are B cells (B220^{+}), macrophages (F4/80^{+}) or DCs (CD11c^{+}). Data shows average of the percentages counted in 10 random high power fields (hpf; *: $p < 0.05$, student's *t*-test). (**C**) Flow cytometry analysis of the MHCII^{+} myeloid cells in the breast tumors demonstrates the majority of MHCII^{+} CD11c^{+} DCs to express CD11b^{+} in PyMT^{tg} and K14-TSLP^{tg};PyMT^{tg} breast tumors. Representative flow plots are shown. Note that the breast tumors are from age-matched PyMT^{tg} and K14-TSLP^{tg};PyMT^{tg} female mice at the time point when PyMT^{tg} animals have developed terminal breast cancers.

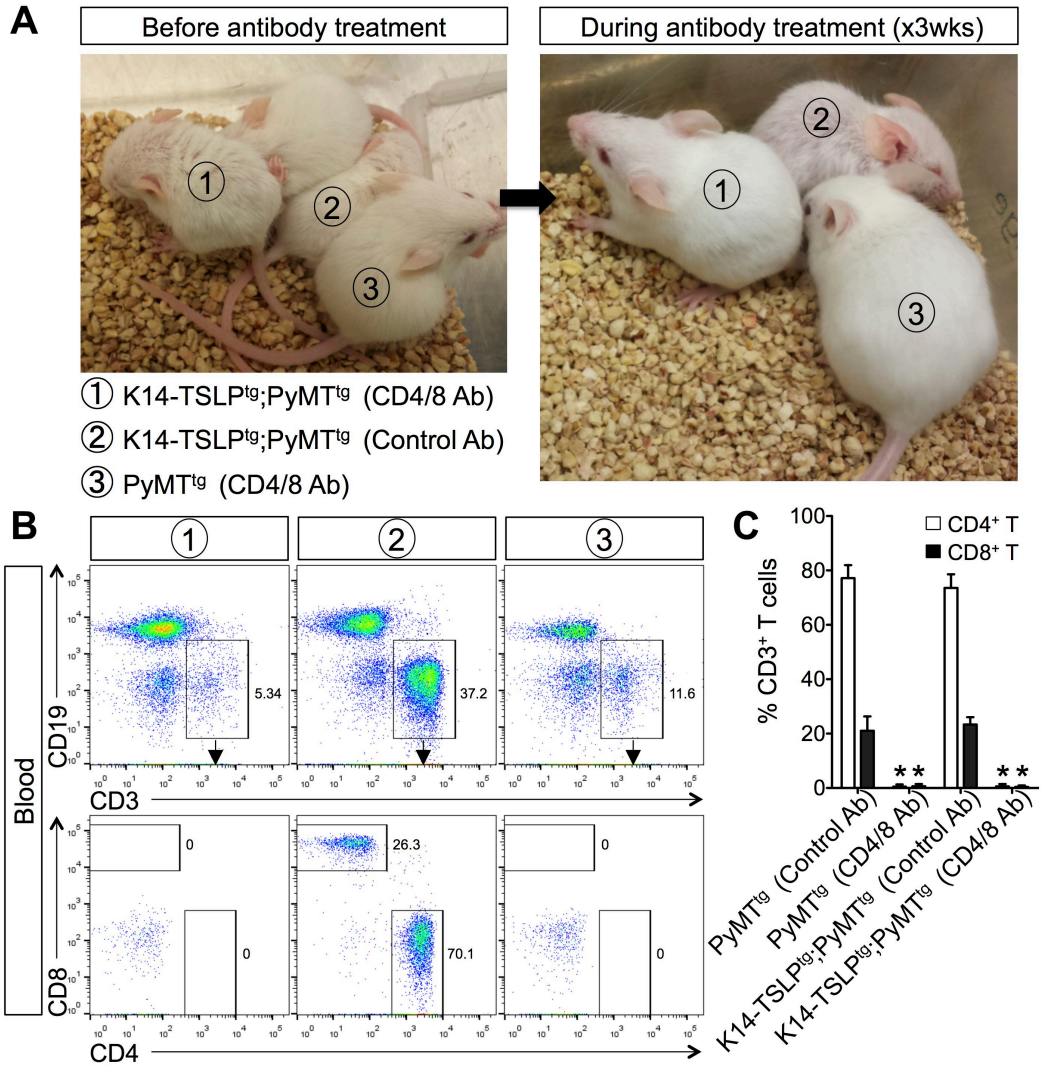

Supplemental Figure 10. Anti-CD4 and anti-CD8 antibody depletion effectively eliminates CD4$^+$ and CD8$^+$ T cells in the periphery and cures the skin rash in K14-TSLP^{tg};PyMT^{tg} mice. (**A**) Shown are representative images of PyMT^{tg} and K14-TSLP^{tg};PyMT^{tg} mice before and 3 weeks after treatment with anti-CD4/8 antibody (#1 and #3) or control antibody (#2). Note the normalization of hair coat in anti-CD4/8 antibody-treated K14-TSLP^{tg};PyMT^{tg} mouse compared to its control antibody-treated K14-TSLP^{tg};PyMT^{tg} littermate. (**B**) Representative flow cytometry plots showing the complete depletion of CD4$^+$ and CD8$^+$ T cells in the peripheral blood of PyMT^{tg} and K14-TSLP^{tg};PyMT^{tg} mice treated with anti-CD4/8 antibody (#1 and #3). (**C**) Bar graph showing the average percentage of peripheral blood CD3$^+$ T cells that are CD4$^+$ or CD8$^+$

T cells in control and anti-CD4/8 antibody-treated animals (*: $p < 0.05$ compared to control antibody-treated groups, student's *t*-test).

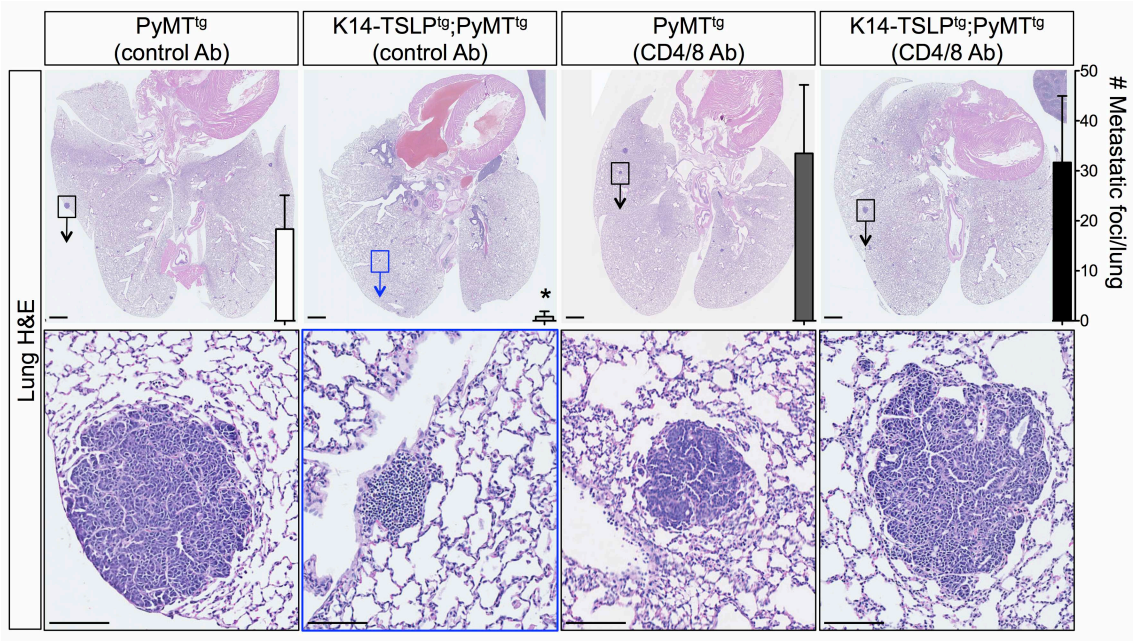

Supplemental Figure 11. K14-TSLP^{tg};PyMT^{tg} mice treated with anti-CD4/8 antibody develop metastatic breast cancer similar to PyMT^{tg} mice. Representative images of H&E-stained lungs of antibody-treated PyMT^{tg}, K14-TSLP^{tg};PyMT^{tg} mice demonstrate the breast cancer metastatic foci in PyMT^{tg} and anti-CD4/8 antibody-treated K14-TSLP^{tg};PyMT^{tg} mice. On the other hand, control antibody-treated K14-TSLP^{tg};PyMT^{tg} mice do not have any breast cancer metastasis to their lungs but show foci of lymphocytic inflammation in their longs associated with their atopic disease (blue inset). Note the higher magnification of metastatic foci marked by black insets. The average numbers of breast cancer metastatic foci per lung section in random sections of 6 lungs from each treatment group are shown as bar graphs at the right edge of each image (*: $p < 0.05$ compared to control antibody-treated PyMT^{tg} mice, student's *t*-test). Scale bars: lung images = 1mm, insets = 100μm.

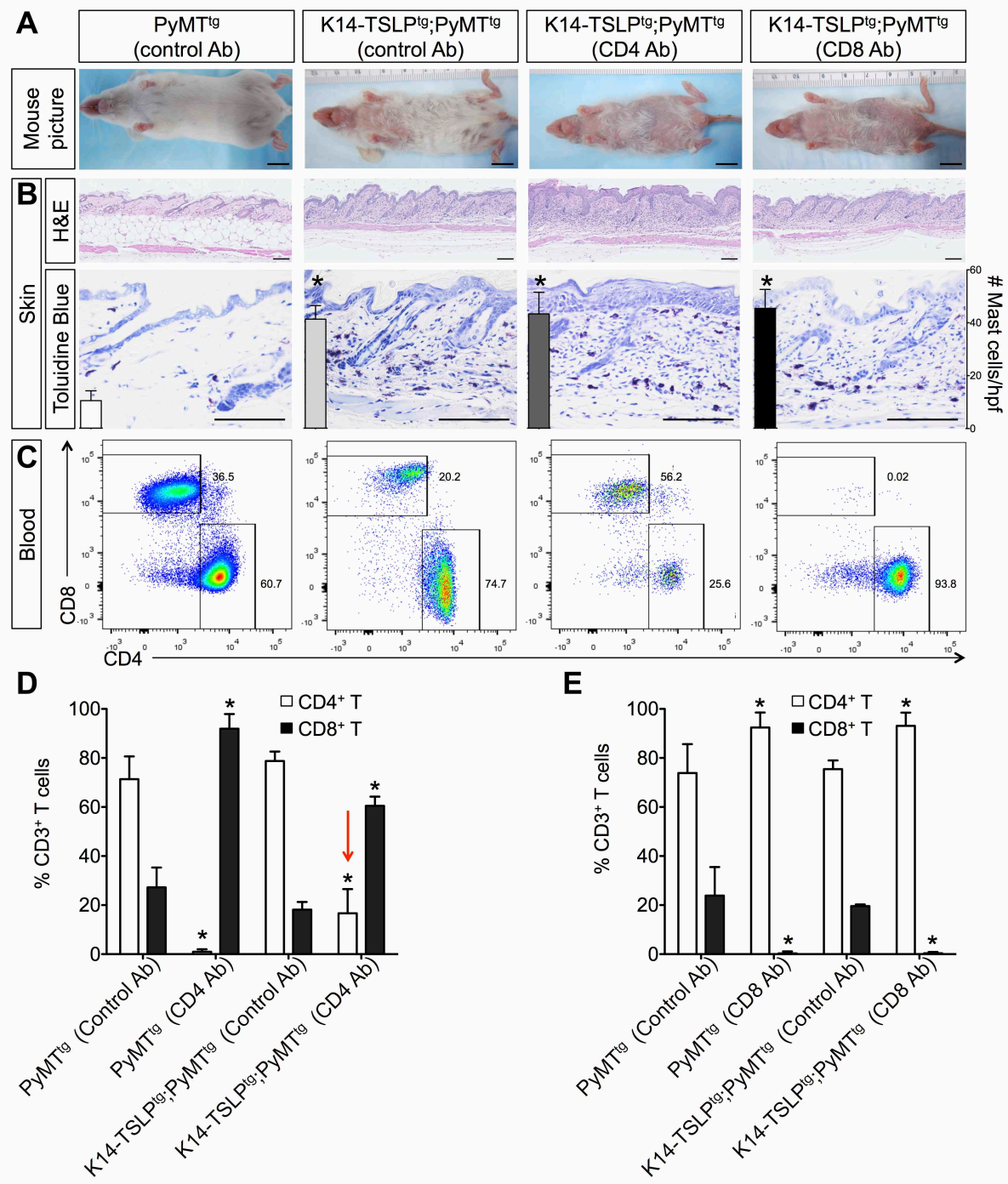

Supplemental Figure 12. Anti-CD4 antibody depletion alone fails to eliminate $CD4^+$ cells in K14-$TSLP^{tg}$;$PyMT^{tg}$ mice, while depletion of $CD8^+$ T cells in K14-$TSLP^{tg}$;$PyMT^{tg}$ mice does not alter their inflammatory skin phenotype. (**A**) Representative images of mice demonstrate the degree of skin rash and hair loss in anti-CD8 antibody-treated K14-$TSLP^{tg}$;$PyMT^{tg}$ mice, which also exists in mice treated with anti-CD4 antibody (Scale bars = 1cm). (**B**) Skin histological

analysis demonstrates the extend of epidermal thickening and dermal inflammation in anti-CD4 or anti-CD8 antibody-treated K14-TSLP^{tg};PyMT^{tg} mice. Shown are representative images of H&E and toluidine blue staining from adult PyMT^{tg} and K14-TSLP^{tg};PyMT^{tg} mice. The average number of mast cells in 10 random high power fields (hpf) are shown as bar graphs next to the images (*: $p < 0.05$ compared to PyMT^{tg}, student's *t*-test; scale bars = 100μm). (**C**) Flow cytometry analysis shows an effective depletion of CD8$^+$ T cells by anti-CD8 antibody but the failure of anti-CD4 antibody to deplete CD4$^+$ T cells in K14-TSLP^{tg};PyMT^{tg} blood. Representative flow cytometry plots are shown. Numbers in the plots indicate %CD3$^+$ T cells within each box. (**D**) Bar graph showing the average percentage of peripheral blood CD3$^+$ T cells that are CD4$^+$ or CD8$^+$ T cells in control and anti-CD4 antibody-treated animals. Note the failure of anti-CD4 antibody to deplete CD4$^+$ T cells in K14-TSLP^{tg};PyMT^{tg} blood (red arrow). (**E**) Bar graph shows the average percentage of peripheral blood CD3$^+$ T cells that are CD4$^+$ or CD8$^+$ T cells in control and anti-CD8 antibody-treated animals (n = 3 in each group; *: $p < 0.05$ compared to control antibody-treated groups, student's *t*-test).

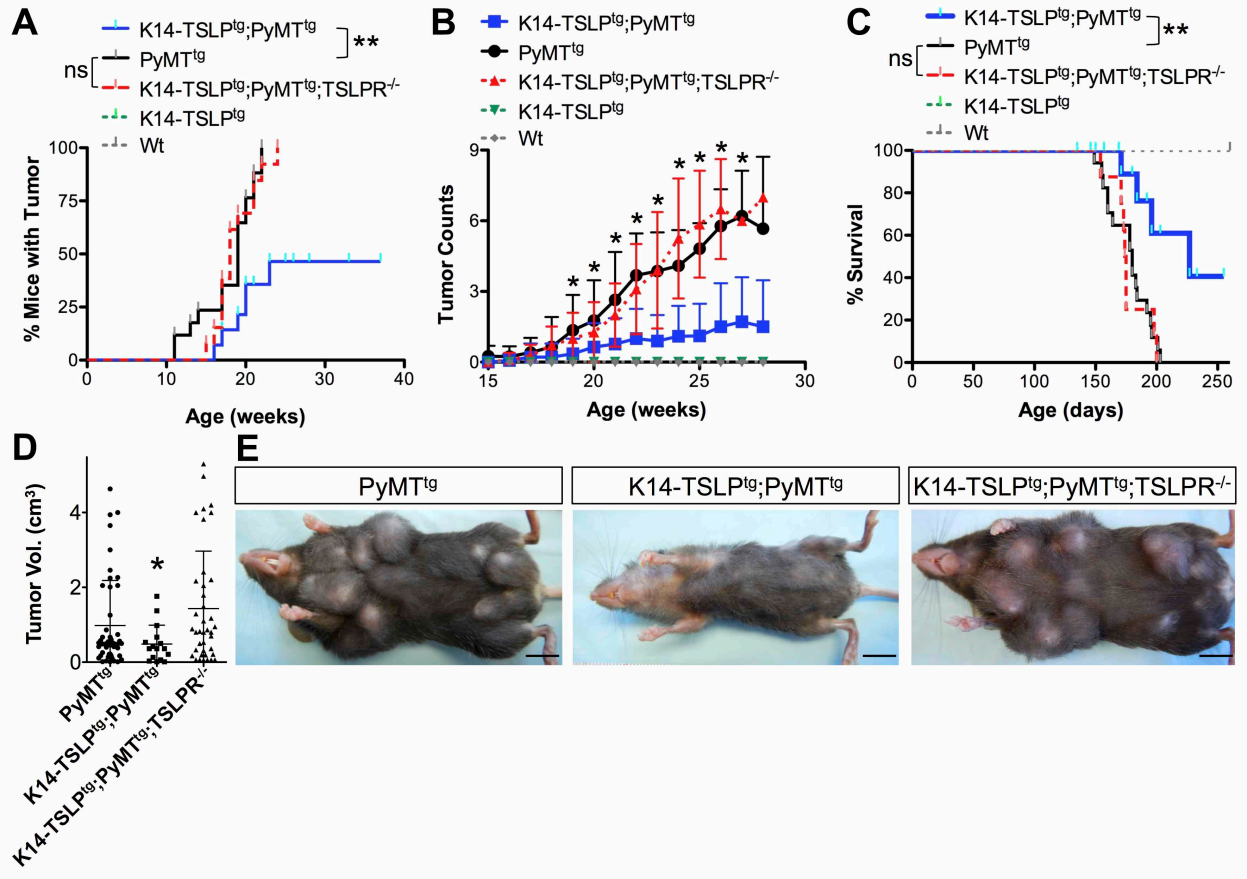

Supplemental Figure 13. Skin TSLP overexpression suppresses breast carcinogenesis in mice maintained on the C57BL/6 background and this tumor-protective effect is eliminated in animals lacking TSLP receptor. (**A**, **B** and **C**) K14-TSLP^{tg};PyMT^{tg} female mice are protected from breast cancer development compared to their PyMT^{tg} and K14-TSLP^{tg};PyMT^{tg};TSLPR$^{-/-}$ counterparts. (**A**) Time to tumor onset, (**B**) the average number of breast tumors per mouse and (**C**) the animals' survival graph are shown (n $\geq$ 13 in each group; **: p <0.001, ns = not significant, log-rank test; *: p < 0.05 starting at week 19 only for K14-TSLP^{tg};PyMT^{tg} compared to PyMT^{tg}, student's t-test). (**D**) Scatter plot compares the average volume of palpable breast tumors in PyMT^{tg}, K14-TSLP^{tg};PyMT^{tg} and K14-TSLP^{tg};PyMT^{tg};TSLPR$^{-/-}$ at the endpoint when PyMT^{tg} mice have developed terminal cancer (*: p < 0.05 compared to PyMT^{tg} group, student's t-test). (**E**) K14-TSLP^{tg};PyMT^{tg} female mice have atopic dermatitis-like skin rash but markedly smaller breast tumors compared to PyMT^{tg} mice. The skin rash and tumor protection are eliminated in

K14-TSLP^{tg};PyMT^{tg};TSLPR$^{-/-}$ mice lacking TSLP reception. Representative images are shown. Error bars indicate SD. Scale bars = 1cm.

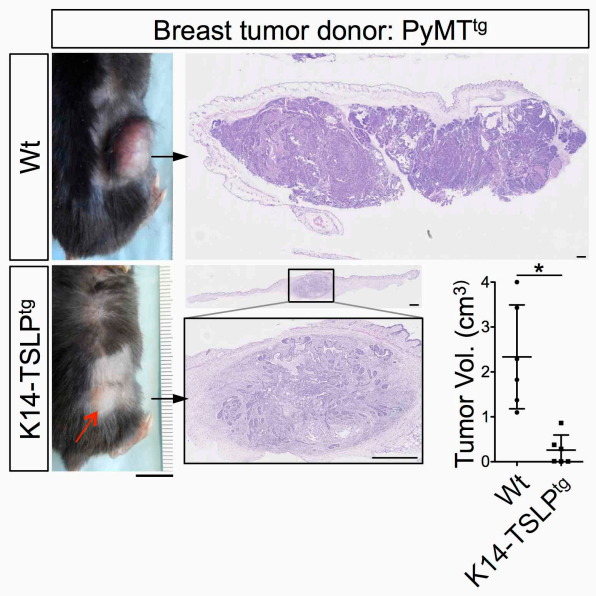

Supplemental Figure 14. PyMT^{tg} primary breast tumors fail to grow in K14-TSLP^{tg} mice. Representative images are shown of animals and H&E-stained breast tumors formed after implanting PyMT^{tg} primary tumor cells into inguinal mammary fat pad of 6- to 8-week-old Wt and K14-TSLP^{tg} mice (red arrow points to a small tumor formed in K14-TSLP^{tg} mouse). Scatter plot shows the average volume of the breast tumors forming in Wt and K14-TSLP^{tg} mice at the endpoint when Wt tumors have reached their terminal volume (n = 6 in each group; *: $p < 0.05$, student's *t*-test). Scale bars: mouse images = 1cm, histology images = 500µm.

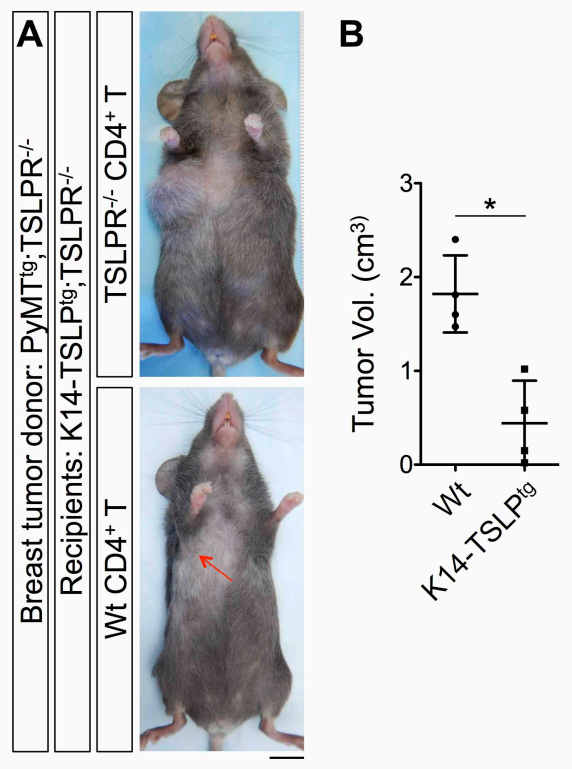

Supplemental Figure 15. TSLP-stimulated Wt CD4^{+} T cells inhibit the growth of breast tumors orthotopically implanted into the thoracic mammary fad pad. (**A**) Shown are representative images of K14-TSLP^{tg};TSLPR$^{-/-}$ mice with their implanted tumors. Red arrow points to a small tumor in K14-TSLP^{tg};TSLPR$^{-/-}$ animal injected with Wt CD4^{+} T cells (Scale bar = 1cm). (**B**) Scatter plot shows the average volume of the breast tumors forming in Wt and K14-TSLP^{tg} mice at the endpoint when Wt tumors have reached their terminal volume (n = 4 in each group; *: $p < 0.05$, student's *t*-test).

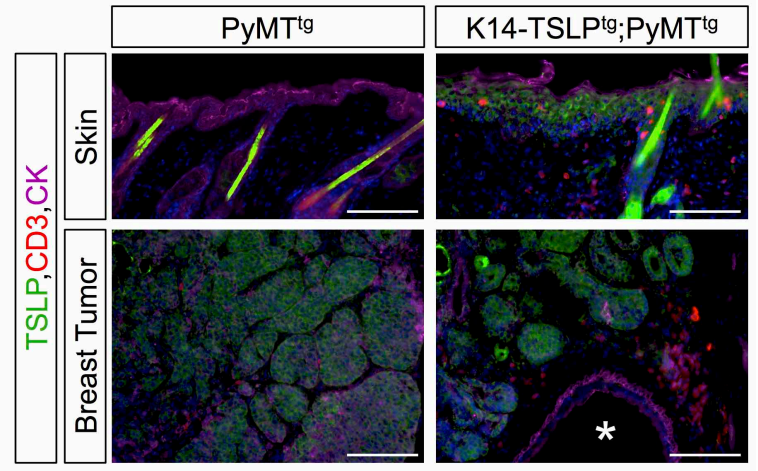

Supplemental Figure 16. TSLP is expressed in the skin keratinocytes of K14-TSLP^{tg};PyMT^{tg} mice and the breast tumors of both PyMT^{tg} and K14-TSLP^{tg};PyMT^{tg} mice at the age when PyMT^{tg} mice have reached the terminal stage of their cancer. Shown are representative images of TSLP/CD3/Cytokeratin (CK) immunofluorescent stains of the skin and breast tumors. Asterisk highlights a dilated mammary duct in K14-TSLP^{tg};PyMT^{tg} breast tumor, which lacks any detectable TSLP expression in its epithelial lining (Scale bars = 100μm).

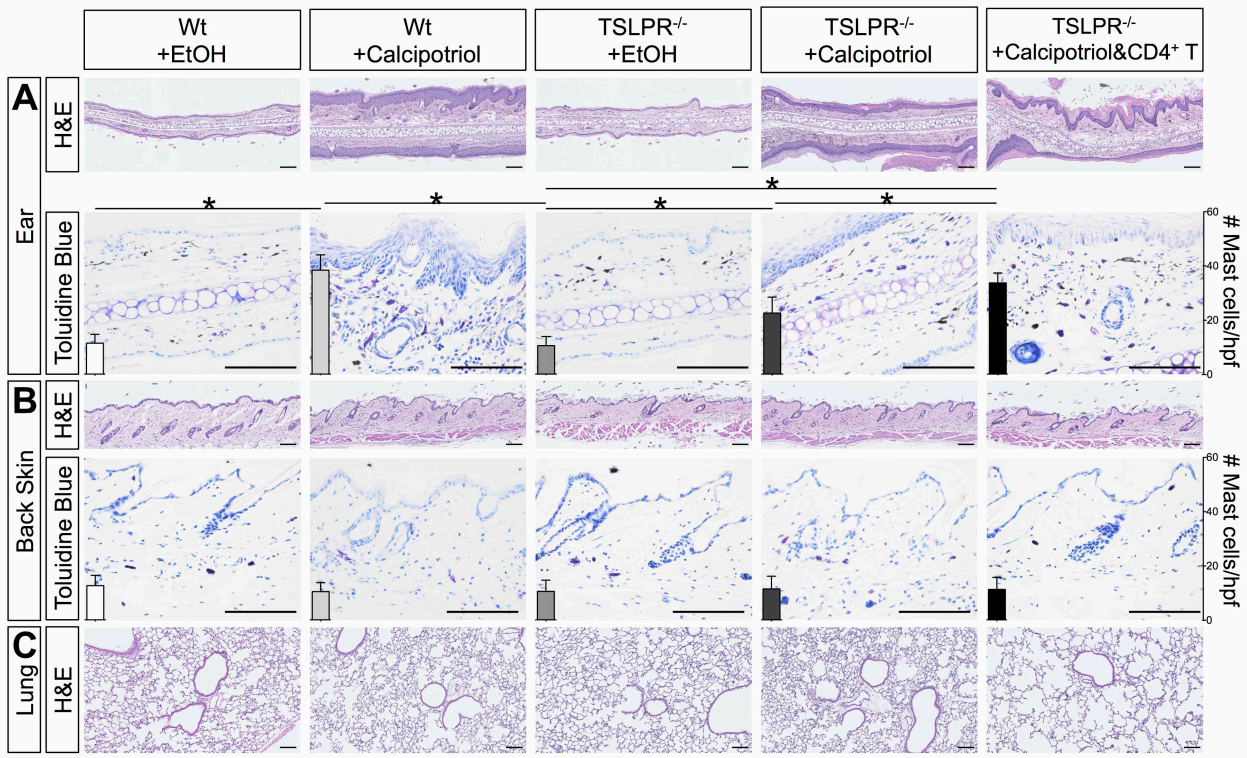

Supplemental Figure 17. Calcipotriol application to the mouse ears causes a localized inflammation in the ears but does not result in allergic inflammation at other barrier sites. (**A**) Ear swelling, epidermal thickening, dermal inflammatory infiltrate including the accumulation of mast cells are present in ears of Wt mice treated with calcipotriol and TSLPR$^{-/-}$ mice that received Wt CD4^{+} T cells and calcipotriol. This local inflammation is significantly less pronounced in TSLPR$^{-/-}$ mice that only received calcipotriol and absent in mice treated with EtOH in their ears. Representative images of H&E- and toluidine blue-stained ear sections are shown. The average number of mast cells in 10 random hpf are shown as bar graphs next to the images (*: $p < 0.05$, student's *t*-test). (**B**) Back skin of the mice in all groups are normal and show no sign of allergic inflammation including no increase in dermal mast cell counts. Representative images are shown. The average number of mast cells in 10 random hpf are shown as bar graphs next to the images. (**C**) Lungs of the animals in all the treatment groups are not affected by calcipotriol

treatment and there is no sign of inflammation in the lungs. Representative images show the H&E-stained lung airways. Scale bars =100μm.

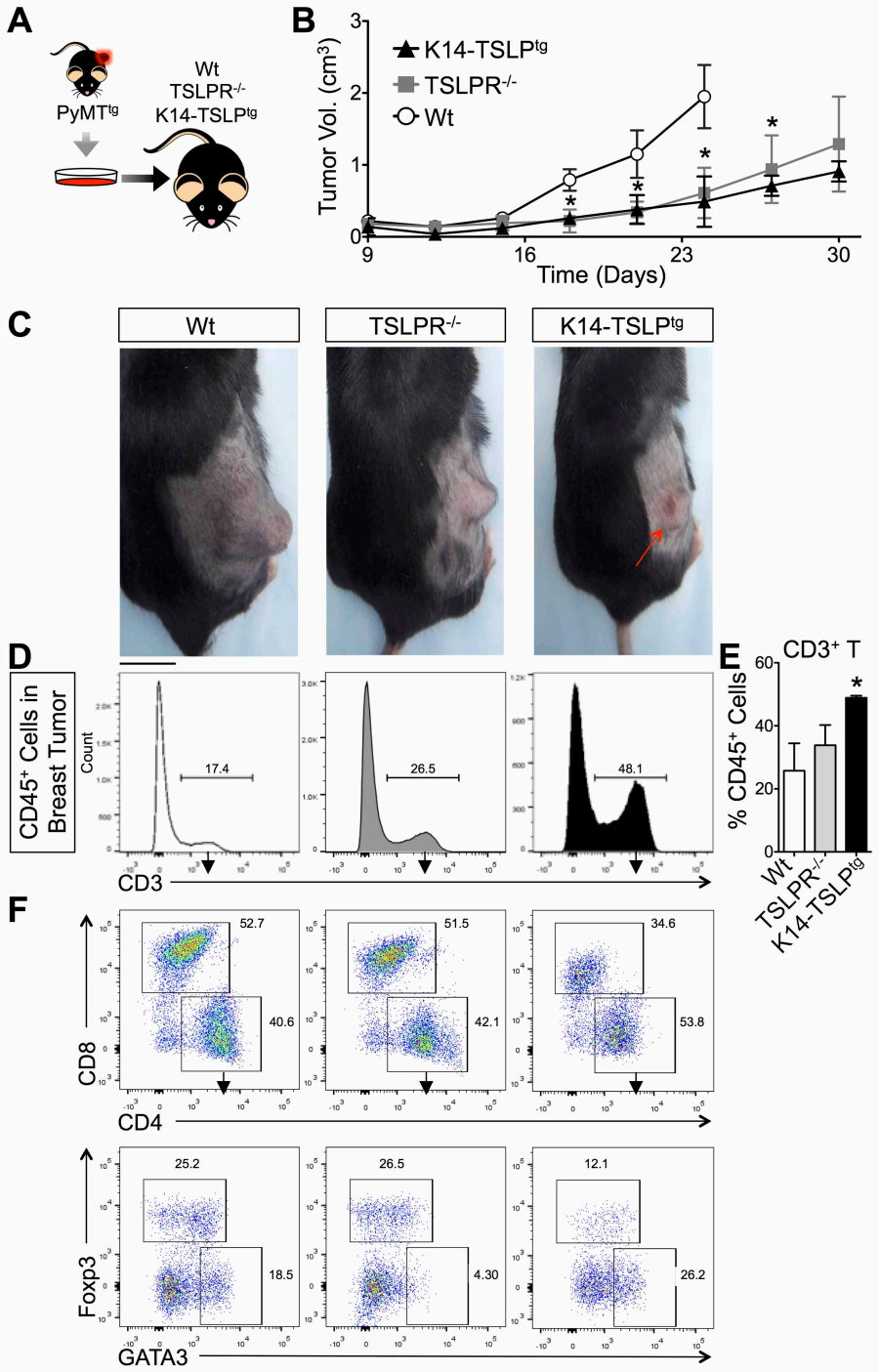

Supplemental Figure 18. High systemic TSLP levels induce anti-tumor immunity against cell line-derived breast cancers. (**A**) Schematic diagram depicts the development of cell line from a PyMT^{tg} breast tumor and its orthotopic implantation into the mammary fat pad of 6- to 8-week-old Wt, TSLPR$^{-/-}$ and K14-TSLP^{tg} mice. (**B**) Graph shows the average volume of tumors in Wt,

TSLPR$^{-/-}$ and K14-TSLP^{tg} mice over time (n = 3 in each group; *: $p < 0.05$ for both TSLPR$^{-/-}$ and K14-TSLP^{tg} compared to Wt controls, student's *t*-test). (**C**) Shown are representative images of breast cancers forming from implantation of PyMT^{tg} cell line in inguinal mammary fat pad of Wt, TSLPR$^{-/-}$ and K14-TSLP^{tg} female mice. Red arrow points to a small tumor formed in K14-TSLP^{tg} mouse. (**D**) Flow cytometry analysis demonstrates that a higher percentage of tumor infiltrating CD45^{+} leukocytes are CD3^{+} T cells in K14-TSLP^{tg} mice. Representative flow cytometry plots are shown. Numbers in the plots indicate the percentage of CD45^{+} cells that are T cells. (**E**) Bar graph shows the average T cell density in the tumors as %CD45^{+} leukocytes present within the tumors, based on flow cytometry data (*: $p < 0.05$ compared to Wt, student's *t*-test). (**F**) Characterization of the tumor infiltrating T cells demonstrates that there is a dominant population of CD4^{+} T cells in K14-TSLP^{tg} tumors. Foxp3, GATA3 and T-bet transcription factor staining are shown. Although tumor infiltrating CD4^{+} T cells in both Wt and K14-TSLP^{tg} mice are Th2-polarized (GATA3^{+} CD4^{+} T cells), they are at highly enriched in K14-TSLP^{tg} tumors. Representative flow cytometry plots are shown. The numbers in the plots indicate the percent of all T cells (upper panel) or CD4^{+} T cells (lower panel) that are within each box. Scale bar equals 1cm.

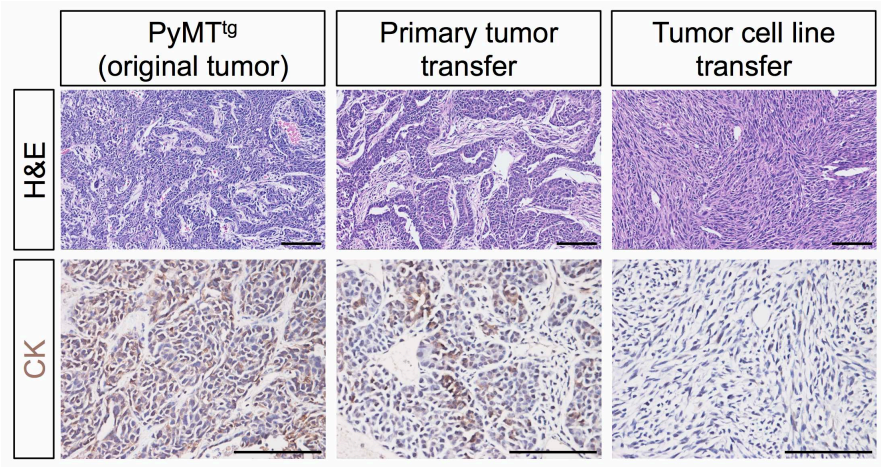

Supplemental Figure 19. Tumors generated by implanting breast cancer cell lines lack the characteristics of the original cancer. The original breast tumors developed in PyMT^{tg} mice are similar to the tumors develop from implantation of primary tumor cells. In stark contrast to these, the tumors formed from a PyMT^{tg} breast tumor cell line are spindle shaped and have lost the cytokeratin (CK) expression, which is the hallmark of the epithelial differentiation (3). Therefore, cell line-derived tumors resemble poorly differentiated metastatic cancers. Representative images are shown (Scale bars = 100μm).

References:

1. Demehri, S., Cunningham, T.J., Hurst, E.A., Schaffer, A., Sheinbein, D.M., and Yokoyama, W.M. 2014. Chronic allergic contact dermatitis promotes skin cancer. *J Clin Invest* 124:5037-5041.
2. Hingorani, S.R., Petricoin, E.F., Maitra, A., Rajapakse, V., King, C., Jacobetz, M.A., Ross, S., Conrads, T.P., Veenstra, T.D., Hitt, B.A., et al. 2003. Preinvasive and invasive ductal pancreatic cancer and its early detection in the mouse. *Cancer Cell* 4:437-450.
3. Franke, W.W., Weber, K., Osborn, M., Schmid, E., and Freudenstein, C. 1978. Antibody to prekeratin. Decoration of tonofilament like arrays in various cells of epithelial character. *Exp Cell Res* 116:429-445.